High-Resolution X-ray Structure of the Unexpectedly Stable Dimer of the [Lys$^{(-2)}$-Arg$^{(-1)}$-des(17−21)]Endothelin-1 Peptide‡

François Hoh,§ Rachel Cerdan,§ Quentin Kaas,§ Yoshinori Nishi,|| Laurent Chiche,§ Shigeru Kubo,⊥ Naoyoshi Chino,⊥ Yuji Kobayashi,|| Christian Dumas,§ and André Aumelas*,§

Centre de Biochimie Structurale, UMR5048 CNRS-Université Montpellier I, UMR554 INSERM-Université Montpellier I, Faculté de Pharmacie, 15 avenue Charles Flahault, BP 14491, 34093 Montpellier-Cedex 5, France, Peptide Institute, Inc., 4-1-2 Ina, Minoh, Osaka 562-8686, Japan, and Graduate School of Pharmaceutical Sciences, Osaka University, 1-6 Yamadaoka, Suita, Osaka 565-0871, Japan

Received May 4, 2004; Revised Manuscript Received September 20, 2004

ABSTRACT: Previous structural studies on the [Lys$^{(-2)}$-Arg$^{(-1)}$]endothelin-1 peptide (KR-ET-1), 540-fold less potent than ET-1, strongly suggested the presence of an intramolecular Arg^{-1}−Asp^{8} (R^{-1}−D^{8}) salt bridge that was also observed in the shorter [Lys$^{(-2)}$-Arg$^{(-1)}$-des(17−21)]endothelin-1 derivative (KR-CSH-ET). In addition, for these two analogues, we have shown that the Lys-Arg dipeptide, which belongs to the prosequence, significantly improves the formation of the native disulfide bonds (≥96% instead of ≈70% for ET-1). In contrast to what was inferred from NMR data, molecular dynamics simulations suggested that such an intramolecular salt bridge would be unstable. The KR-CSH-ET peptide has now been crystallized at pH 5.0 and its high-resolution structure determined *ab initio* at 1.13 Å using direct methods. Unexpectedly, KR-CSH-ET was shown to be a head-to-tail symmetric dimer, and the overall interface involves two intermolecular R^{-1}−D^{8} salt bridges, a two-stranded antiparallel β-sheet, and hydrophobic contacts. Molecular dynamics simulations carried out on this dimer clearly showed that the two intermolecular salt bridges were in this case very stable. Sedimentation equilibrium experiments unambiguously confirmed that KR-ET-1 and KR-CSH-ET also exist as dimers in solution at pH 5.0. On the basis of the new dimeric structure, previous NMR data were reinterpreted. Structure calculations were performed using 484 intramolecular and 38 intermolecular NMR-derived constraints. The solution and the X-ray structures of the dimer are very similar (mean rmsd of 0.85 Å). Since the KR dipeptide at the N-terminus of KR-CSH-ET is present in the prosequence, it can be hypothesized that similar intermolecular salt bridges could be involved in the *in vivo* formation of the native disulfide bonds of ET-1. Therefore, it appears to be likely that the prosequence does assist the ET-1 folding in a chaperone-like manner before successive cleavages that yield the bioactive ET-1 hormone.

Discovered in 1988, endothelin (ET-1)[1] is a disulfide-bonded hormone (21 amino acids, including four cysteines) that possesses a strong and long-lasting vasoconstrictor effect on smooth muscles of the vascular system (*1*, *2*). ET-1 is initially expressed as a 212-residue precursor (*3*). Its maturation process consists of both the formation of the correct arrangement of the two disulfide bonds and then the removal of the upstream and downstream sequences by successive enzymatic cleavages. The big ET-1-[1−39] is one intermediary whose molar potency is 140-fold lower than that of ET-1 (*4*).

ET-1 has been chemically synthesized, and whatever method was used, the oxidative folding step yielded at least 25% of the non-native disulfide isomer (*5*). The ET-1 structure has been determined first by NMR (*6*−*9*) and then by X-ray diffraction (*10*). It mainly consists of an α-helix (residues 9−16) tightly linked to an extended strand (residues 1−3) by the 1−15 and 3−11 disulfide bonds giving rise to the cystine-stabilized helical motif (CSH) (*11*, *12*). The C-terminal part (residues 17−21) was poorly defined in the solution structures but helical in the crystal structure (*10*).

A large number of analogues have been synthesized and revealed that the D^{8}, Y^{13}, L^{17}, and W^{21} residues as well as the native disulfide bond arrangement (C^{1}−C^{15} and C^{3}−C^{11}) were all essential for the expression of the vasoconstrictor activity (*13*). Among these analogues, the [Lys$^{(-2)}$-Arg$^{(-1)}$]-ET-1 peptide (KR-ET-1), extended on its N-terminal part by two residues belonging to its prosequence (K^{51} and R^{52},

‡ The coordinates of the X-ray structure have been deposited in the Protein Data Bank as entry 1T7H.

* To whom correspondence should be addressed: Centre de Biochimie Structurale, UMR 5048 CNRS-UM1/UMR 554 INSERM-UM1, Faculté de Pharmacie, 15 avenue Charles Flahault, 34093 Montpellier Cedex 5, France. Telephone: 33 467 043 432. Fax: 33 467 529 623. E-mail: aumelas@cbs.cnrs.fr.

§ UMR5048-CNRS-Université Montpellier I.

|| Osaka University.

⊥ Peptide Institute, Inc.

[1] Abbreviations: 1D, one-dimensional; 2D, two-dimensional; 3D, three-dimensional; ADPs, anisotropic displacement parameters; CSH, cystine-stabilized helical motif; COSY, correlated spectroscopy; ET-1, endothelin; GB, generalized Born; KR-ET-1, [Lys$^{(-2)}$-Arg$^{(-1)}$]-endothelin-1; KR-CSH-ET, [Lys$^{(-2)}$-Arg$^{(-1)}$-des(17−21)]endothelin-1; NMR, nuclear magnetic resonance; NOE, nuclear Overhauser effect; NOESY, nuclear Overhauser effect spectroscopy; PME, particle-mesh Ewald; rmsd, root-mean-square deviation; SRTb, sarafotoxin-S6b; TOCSY, total correlated spectroscopy; TSP-d_4, sodium 2,2,3,3-tetradeuterio-3-(trimethylsilyl)propionate.

10.1021/bi049098a CCC: $27.50
Published on Web 11/10/2004

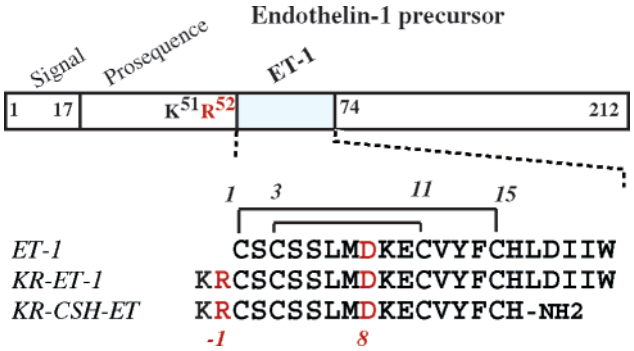

FIGURE 1: Scheme of the human endothelin-1 precursor and sequences of KR-ET-1 and of KR-CSH-ET showing the disulfide pattern as well as the numbering that was used. Since the Lys-Arg dipeptide belongs to the prosequence, the KR residues are numbered in a reverse way. Residues R^{-1} and D^{8} involved in a salt bridge are colored red. The KR-CSH-ET peptide results in the removal of five residues and of the addition of the upstream KR residues of the prosequence at the C-terminal and N-terminal parts of ET-1, respectively.

Figure 1), was 540 times less potent than the parent peptide, although the ET-1 sequence itself was unchanged. In contrast, the addition of the Lys and Arg residues gave an unexpectedly high yield (>96%) of the native disulfide isomer instead of ≈70% for the parent peptide (*14*−*16*) (Figure 1).

To understand the involvement of this dipeptide in the improvement of the formation of the native disulfide isomer, a structural study was carried out by CD and ^{1}H NMR spectroscopies (*17*). First, we observed large and unusual spectral changes depending on the ionization state of the carboxyl groups, and second, we demonstrated that the Asp^8 side chain was involved in a salt bridge with the Arg^{-1} side chain by using point mutations. The large spectral changes were interpreted on the basis of two conformers in slow exchange due to the presence or absence of the R^{-1}−D^8 intramolecular salt bridge. We demonstrated that this salt bridge was still observed in the chimeric [Lys-Arg]Sarafotoxin analogue (KR-SRTb) (*18*). Since ET-1 and SRT sequences belong to the same family, but differ from both their C-terminal part (residues 17−21) and their loop sequence (residues 4−7), we inferred that the sequences of these two segments are not essential for salt bridge stability. The fact that the C-terminal part of ET-1 is not critical for salt bridge stability was recently supported by the study of the [Lys-Arg-des(17−21)]ET-1 truncated analogue (KR-CSH-ET). This peptide exhibits a pH-dependent behavior very similar to that of the KR-ET-1 parent peptide, strongly suggesting the presence of an analogous R^{-1}−D^8 salt bridge.

The NMR data implied a remarkably stable and populated R^{-1}−D^8 salt bridge in solution at pH >4. Surprisingly, however, this salt bridge appeared to be particularly unstable in molecular dynamics simulations performed using either an implicit solvation scheme (seven 2 ns simulations) or an explicit solvation and the particle-mesh Ewald method for calculating long-range electrostatic interactions (one 5 ns simulation) (*19*). In all eight simulations, (i) the R^{-1}−D^8 salt bridge was rapidly lost, (ii) the conformation significantly deviated from the starting NMR structure, and (iii) the energy dropped by ∼10−30 kcal/mol. Even though the R^{-1}−D^8 salt bridge reappeared part of the time in two of eight simulations, clear discrepancies were thus apparent between structures calculated from experimental data and the simulations. Whether these discrepancies were due to a deficiency of the molecular dynamics simulations or to a partial misinterpretation of experimental data remained to be determined. Indeed, standard ^{1}H NMR methods cannot provide proton−proton constraints directly accounting for an R−D salt bridge (*20*) since the R HH1 and HH2 protons are quickly exchanged and are thus usually not observed or in some cases are observed as broad signals at low temperatures. Moreover, whatever the conformation of the R−D salt bridge, all nonexchangeable protons of the Arg side chain are more than 0.45 nm from β-protons of Asp, and therefore, no NOE between the two side chains can be used to characterize the interaction. This holds for all representative Arg-Asp conformations in the Atlas of Protein side-chain interactions (http://www.biochem.ucl.ac.uk/bsm/sidechains). For all these reasons, the geometry of the R^{-1}−D^8 salt bridge could not be directly characterized from NMR data, and was inferred from structure calculations. The discrepancy between experimental data and simulations suggested that either the salt bridge could adopt a structure or geometry different from that we have proposed or the force field was unsuitable for properly simulating a solvent-exposed salt bridge.

This is the reason why, to go further into the understanding of the discrepancy prompting our previous study, new experimental approaches were used to unambiguously characterize the overall structure of the peptide and in particular the structure of this salt bridge.

In this paper, we report the crystal structure of the KR-CSH-ET peptide at atomic resolution and apparent molecular mass measurements by analytical ultracentrifugation. On the basis of the X-ray structure, NMR data were reinterpreted and the solution structure of the dimer was calculated. It is shown that, above pH 4, the KR-CSH-ET peptide unexpectedly exists as a symmetric dimer stabilized by two intermolecular salt bridges, a hydrogen bond network, and hydrophobic interactions, both in the crystal and in solution.

In contrast to previous simulations of the monomer (with an intramolecular salt bridge) (*19*), new molecular dynamics simulations performed on the dimer revealed very stable intermolecular salt bridges with no significant structural deviation in the simulations. Altogether, these results now reconcile experiments and simulations. The structure of the dimer will be described, and the reasons for its surprisingly high stability will be discussed. Since such a salt bridge was not observed in the non-native isomer of KR-ET-1 (*21*), we suspect that the high stability of the dimer is responsible for the improvement of the formation of the native disulfide isomer in the thermodynamically controlled step of oxidative folding. Finally, since a cascade of processing is involved in maturation of ET-1 from its precursor, we hypothesize that *in vivo*, a similar salt bridge between the prosequence and ET-1 would assist in the formation of the native disulfide bonds before the successive enzymatic cleavages yielding the active hormone.

EXPERIMENTAL PROCEDURES

Peptide Synthesis and Disulfide Bond Formation. The CSH-ET-1 and KR-CSH-ET-1 peptides were synthesized by using the solid phase strategy according to the previously described scheme (*5*, *14*).

NMR. Samples were prepared by dissolving lyophilized peptides (1.7 mg) in 0.45 mL of a 95% H_2O/5% ^2H_2O

mixture (v/v). The peptide concentration of the resulting sample was ~1.8 mM, and the pH was adjusted by addition of dilute HCl or NaOH. All ^{1}H NMR spectra were recorded on a Bruker AMX-600 spectrometer, and TSP-d_4 was used as an internal reference. The 1D spectra as a function of pH were acquired at 27 °C with either the "Jump and Return" or the "watergate" sequences to observe signals of exchangeable protons (*22*, *23*). 2D experiments, COSY, TOCSY (spin lock of 80 ms), and NOESY (mixing time of 150 ms), were recorded at 7 °C and pH 4.5.

^{1}H NMR spectra of KR-CSH-ET as a function of peptide concentration were recorded in the range of 1.6−0.016 mM at pH 5.5.

Crystallization and Data Collection. Crystals of KR-CSH-ET were obtained by the hanging drop vapor diffusion method. Initial screening was performed using Crystal Screen 1 from Hampton Research (Laguna Niguel, CA). Selected conditions have a pH in the range of 4.6−5.6 to preserve the salt bridge. Small crystals were observed under condition 40 [0.1 M trisodium citrate (pH 5.6), 20% 2-propanol, and 20% PEG 4000]. This starting condition was further refined [0.1 M trisodium citrate, 25% PEG 8000, and 20% 2-propanol (pH 5.0)], and diffraction-quality crystals grew at 18 °C after 4−5 days to average dimensions of 0.1 mm × 0.1 mm × 0.05 mm. Hanging drops were prepared by mixing 1 μL of the peptide solution (10 mg/mL) with an equal volume of the reservoir solution. They were equilibrated against 0.5 mL of reservoir solution.

Before data collection, the crystals were transferred to a cryoprotectant mother liquor supplemented with 30% glycerol and flash-frozen in liquid nitrogen. High-quality diffraction data were collected on a single cryocooled crystal (100 K) using a MarCCD area detector at ESRF (Grenoble, France) beamline BM14. The wavelength was set to 0.80 Å and the crystal-to-detector distance to 76 mm. Two data sets to maximum resolution of 1.13 Å (30 s exposure time) and 2.28 Å (3 s exposure time) were autoindexed and processed with DENZO (*24*). Scaling and merging were performed in SCALA from the CCP4 suite (*25*). The $R_{merge}(I)$ for the data was 7.0%, and the crystal mosaicity refined to 0.3°. The diffraction data statistics are summarized in Table 1. The crystal belongs to the orthorhombic $P2_12_12$ space group, and the unit cell volume suggested a content of two peptide molecules per asymmetric unit with 33% solvent. An overall B factor of 9.1 Å^2 was estimated from the Wilson plot using TRUNCATE (CCP4).

Structure Determination. The initial ambiguity of the asymmetric unit content was solved by selecting the most probable low solvent content (33%) frequently compatible with a high diffracting power and suggesting the presence of two independent molecules. Attempts to determine the structure by preparing isomorphous heavy-atom derivatives and by molecular replacement with AmoRe (*26*), Molrep (*27*), and EPMR (*28*), using as a probe either the X-ray model of native endothelin-1 (PDB entry 1EDN) (*10*) or NMR models (PDB entry 1EDP) (*8*), were unsuccessful. Ultimately, the structure was determined by direct methods using the *ab initio* dual-space recycling procedure called the Shake and Bake method (*29*, *30*) and implemented in the SnB-2.2 program (*31*). Normalized structure factor magnitudes ($|E|$) were computed using DREAR (*32*). The 3156 reflections with the highest $|E|$ values were used to generate 71 000 triplet structure invariants; 1000 trial structures were generated and subjected to 180 cycles of the SnB phase refinement procedure. A total of approximately 320 peaks were selected from the E maps for real-space recycling. Of the 1000 random sets of trial phases that were processed, 40−55 yielded possible solutions. One of the most successful trials at 1.13 Å data, with an R_{min} of 0.458, was examined in detail. The phases and map were calculated using the top 320 peaks. The corresponding map was of high quality and included peaks corresponding to nearly all of the 300 non-hydrogen atoms of the two peptidic molecules.

Table 1: Statistics on Data Collection and Refinement[a]

Data Collection	
space group	$P2_12_12$
a (Å)	30.14
b (Å)	53.93
c (Å)	19.49
resolution (Å)	18.3−1.13
no. of measured reflections	113786
no. of unique reflections	12081 (903)
$R_{merge}(I)$ (%)	7.0 (28.7)
redundancy	9.3 (3.5)
completeness (%)	99.2 (97.1)
$\langle I/\sigma(I)\rangle$	10.7 (3.1)
Refinement Statistics	
resolution range (Å)	10.0−1.13
no. of reflections (total/free)	12054/613
R_{fac} (including test reflections) (%)	12.0
R_{work} (%)	11.9 (14.9)
R_{free} (%)	13.4 (16.5)
rejection criteria	none
no. of atoms	
protein	307
water	58
B factors (Å^2)	
main chain atoms	7.2
side chain atoms	11.2
overall protein/water	9.3/21.3
rmsd from ideal values	
bond distances (Å)	0.02
bond angles (deg)	1.93
chiral volumes (Å^3)	0.13
Ramachandran plot	
most favored (%)	93.8
allowed (%)	6.2

[a] Values in parentheses are for the outer resolution shell (1.13−1.16 Å).

Model Building and Refinement. The complete atomic model of the two molecules of the asymmetric unit was built using the automatic tracing and refinement Arp/wArp procedure (*33*). All structure factor refinements were performed in Refmac5 (*34*). Reflections in the range of 23−10 Å were not included because of overflow and high background problems during data collection. A random 4.9% subset of the reflections was selected for the R_{free} testing (*35*). Model adjustments performed in O (*36*) were based on $2mF_o - DF_c$ and $mF_o - DF_c$ electron density maps (*37*). The initial refinement, including the two peptide molecules, started with 2.5 Å data, but the resolution was quickly extended in a stepwise procedure to include all the reflections in the range of 10.0−1.13 Å without any σ cutoff and without noncrystallographic constraints. The weighting parameter between the X-ray and geometric part of the refinement residual was gradually increased from 1 to 5 to untighten the stereochemical constraints. All additional peaks in electron density maps were included as water molecules or to model alternate side

chain conformations. The occupancies of dual conformations were estimated by analyzing residual peaks in $mF_o - DF_c$ electron density maps. Protein hydrogen atoms were introduced at calculated positions and not refined. The favorable data-to-parameter ratio at atomic resolution made possible the refinement of individual anisotropic displacement parameters (ADPs). Several rounds of refinement were performed to introduce restrained ADPs for the peptide atoms and reduced R_{work} by 2.3% and R_{free} by 2.1%. Further solvent waters were added. The final refinement steps in which the test reflections were included converged at an *R* factor value of 12.0% for all reflections. The refinement statistics are summarized in Table 1.

Final Model. The final structure refined at cryogenic temperature contains all atoms for the two peptidic molecules and 58 water molecules. The electron density map for five side chains clearly showed the presence of two alternate conformations (see Results). The stereochemistry, geometry, and quality of the structure were assessed using PROCHECK (*38*), SFCHECK (*39*), and PARVATI (*40*). The Ramachandran plot shows 93.8 and 6.2% of residues in the core and allowed regions, respectively. The coordinates of the KR-CSH-ET peptide crystal structure and the structure factors have been deposited in the RSCB Protein Data Bank (entry 1T7H).

Analytical Ultracentrifugation. Sedimentation equilibrium experiments were performed with a Beckman Optima XL-I analytical ultracentrifuge using double-sector centerpieces and sapphire windows, at 45 000 rpm and 20 °C. The KR-ET-1 and KR-CSH-ET peptides were dissolved at concentrations of 0.1−4.0 mg/mL in 0.2 M sodium carbonate buffer (pH 9.7), 0.2 M acetate buffer (pH 5.0), and 0.2 M hydrochloric acid (pH 1.4), including 50 mM NaCl. Absorbance scans at 280 nm were measured in the radial step mode at 0.001 cm intervals, and data were collected taking the average of 16 measurements at each radial distance. The approach to equilibrium was considered to be complete when replicate scans separated by ≥6 h were indistinguishable. The molecular extinction coefficients at 280 nm of KR-ET-1 (7210 M^{-1} cm^{-1}) and of KR-CSH-ET (1520 M^{-1} cm^{-1}) were calculated by using the program at the http://www.expasy-.org/tools/protparam.html web site. Their partial specific volumes (0.726 cm^3/g for KR-ET-1 and 0.704 cm^3/g for KR-CSH-ET) were estimated from the amino acid composition by the method of Cohn and Edsall (*41*). The density of the solvent was assumed to be 1.00 g/cm^3.

From sedimentation equilibrium experiments, a weight-average molecular mass is estimated by the following equation (*42*−*44*):

$$M_{app} = \frac{2RT}{(1 - \bar{\nu}\rho)\omega^2} \frac{d(\ln c)}{d(r^2)} \quad (1)$$

where *r* is the radius, *c* is the concentration of the sample, $\bar{\nu}$ is the partial specific volume of the sample, ρ is the density of the solvent, ω is the angular velocity of the rotor (in radians per second), *R* is the universal gas constant, *T* is the absolute temperature, and M_{app} is the apparent molecular mass. Thus, the absorbance at a specified wavelength and position in the solution column should be given by

$$A(r) = A(r_0) \exp[M_{app}H(r^2 - r_0^2)] \quad (2)$$

where $A(r)$ represents the absorbance at radius *r* and $A(r_0)$ is the absorbance at r_0, the radius at the meniscus, and

$$H = \frac{(1 - \bar{\nu}\rho)\omega^2}{2RT} \quad (3)$$

Analysis of the data was carried out utilizing Origin 4.1.

The data were best fitted by a single-species model, as indicated by the random distribution of residuals and the small range of 95% confidence intervals. The nonlinear least-squares fitting with eq 2 gave the apparent molecular masses of these peptides. The concentration dependence of the apparent molecular masses of KR-ET-1 and KR-CSH-ET at various pHs was measured within the concentration range of 0.1−4.0 mg/mL. The extrapolation of the molecular mass values to zero concentration gave the weight-average molecular masses of these peptides.

Calculation of the Solution Structure of the KR-CSH-ET Dimer. Structure calculations were performed on a Silicon Graphics Origin 200 workstation. The NOE intensities were classified as strong, medium, and weak, and converted into distance constraints of 2.5, 3.0, and 4.0 Å, respectively. If the connectivity involved side chain protons, 3.0, 4.0, and 5.0 Å upper bounds, respectively, were used instead to account for higher mobility. For sequential $d_{\alpha N}$ and d_{NN} connectivities, we used upper bounds of 2.5, 3.0, and 3.5 Å and 2.8, 3.3, and 4.0 Å, respectively. When necessary, the distance constraints were corrected for pseudoatoms. Φ angles of residues with small or large $^3J_{HN-H\alpha}$ coupling constants (<4 or >8.5 Hz) were constrained in the range of −90° to −40° or −160° to −80°. Disulfide bridges were imposed through distance constraints of 2.0−2.1, 3.0−3.1, and 3.75−3.95 Å on S*i*−S*j*, S*i*−Cβ*j*, S*j*−Cβ*i*, and Cβ*i*−Cβ*j* distances. No hydrogen bond was initially imposed.

3D structures were obtained from the distance and angle restraints using the torsion angle molecular dynamics method available in DYANA (*45*). As described in the tutorial program, the two monomers were linked by an ≈40 Å "invisible" linker (expected distance ≈ 21 Å) to ensure its flexibility and so that no artificial constraint occurs at the linked extremities. For the final calculation of the dimer, 484 NOE-derived distance restraints (106 medium-range and 108 long-range) and 12 ϕ dihedral angles were used as input data. Among the long-range constraints, 38 were intermolecular, including four intermolecular hydrogen bonds responsible for the stability of the β-sheet interface. Sixty conformers were then calculated, and the 10 structures with the lowest violations of the target function were further refined by restrained molecular dynamics as previously described (*19*).

The visual display, the comparison with the crystal structure, and the calculation of rmsd were performed with INSIGHT 97 (Molecular Simulation Inc., San Diego, CA). The Ramachandran analysis was performed with PROCHECK (*38*), and the limits of the secondary structure elements and the van der Waals surfaces were determined with STRIDE (*46*).

Molecular Dynamics Simulations of the X-ray Dimer. Molecular dynamics simulations were performed with the SANDER module of the AMBER 7 suite (*47*), using the all-atom parm94 force field (*48*). According to p*K* values of residues and pH conditions at which NMR experiments (pH 4.5) and crystal growth (pH 5.0) were performed, R^{-1}, K^{-2},

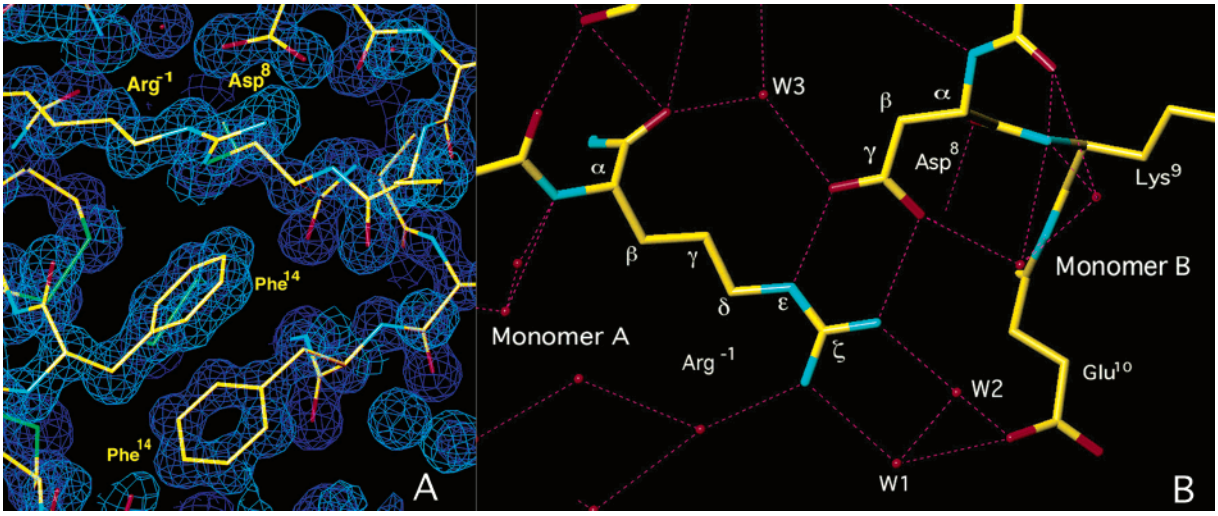

FIGURE 2: X-ray structure of the KR-CSH-ET dimer. (A) The detail of the final electron density map (contoured at the 1.1σ level) at the dimer interface shows the stacking of the phenylalanine rings belonging to each monomer and the R^{-1} and D^8 side chains. (B) Structure of the intermolecular salt bridge. The R^{-1} and D^8 side chains are almost perpendicular. Water molecules are displayed as red spheres and hydrogen bonds as red dashed lines. The presence of the water molecules is discussed in the text.

and K^9 residues were protonated and D^8 and E^{10} residues were deprotonated. H^{16} was protonated at the ND1 position. Several simulations with different initial velocities were performed using the GB/SA implicit solvation scheme (*49*). In addition, a simulation with explicit solvation was performed. The molecule was immersed in a box of TIP3P water molecules (*50*), and the net charge of the protein was neutralized by substitution of three water molecules for chloride ions. Water molecules with the oxygen atom less than 2.40 Å or a hydrogen atom less than 1.80 Å from any protein atom were discarded. The minimum distance from any protein atom and a box edge was 15 Å, resulting in a box containing 4600 water molecules with initial dimensions of 59 Å × 60 Å × 52 Å. Periodic boundary conditions were imposed in all three dimensions. The system was coupled to a heat bath with a temperature T_0 of 298 K and to a pressure bath with a P_0 of 1 atm by applying the algorithm of Berendsen (*51*). A temperature relaxation time t_T of 1 ps and a pressure relaxation time t_P of 0.2 ps were used, and the pressure scaling was anisotropic. A 500 ps MD simulation in which the protein is kept frozen was performed first to equilibrate the water molecules and chloride ions. Then, electrostatic interactions were calculated using the particle-mesh Ewald (PME) summation scheme (*52*), with a cutoff of 10 Å for the separation of the direct and reciprocal space summation and for computation of van der Waals interactions. The covalent bond lengths were kept constant by applying the SHAKE algorithm (*53*), allowing a 1.5 fs time step to be used. Coordinates were saved every 1.5 ps. Analysis of the trajectories was performed with the Ptraj module of the AMBER 7 suite.

RESULTS

Ab Initio Structure Determination and Structure Description. High-diffraction-quality crystals allowed us to determine the structure at the atomic resolution level. Direct methods using Shake and Bake (SnB) yielded solutions for the KR-CSH-ET molecule using 1.13 Å resolution data. Atomic positions for 90% of the two molecules containing 300 non-H atoms, including eight sulfur atoms, were easily interpreted by using the ARP/wARP procedure to automatically build a complete and accurate molecular model. The quality of the final electron density map is illustrated in Figure 2. The refined model is of high precision and includes all atoms of the peptide. The side chains in alternate conformations are modeled without ambiguity: S^5, M^7, and E^{10} in monomer A and S^2 and M^7 in monomer B.

As shown in Figure 3, the overall structure of the peptide consists of an N-terminal extended β-strand (residues C^1−C^3) followed by a loop and a short C-terminal α-helix segment (residues K^9−C^{15}). The engineered N-termini of both molecules present in the asymmetric unit are clearly defined in the electron density map. The side chain of R^{-1} forms an intermolecular salt bridge with the D^8 residue. The stable fold of this peptide is based on the presence of two disulfide bonds. The C^1−C^{15} and C^3−C^{11} disulfide bridges are strongly buried and show standard χ_3 angles: −94.4° and −98.1° for the C^1−C^{15} disulfide bridge (monomers A and B, respectively) and −103.6° and −101.7° for the C^3−C^{11} disulfide bridge, close to the ideal values and nearly the same in the two molecules. The C^3−C^{11} disulfide bond adopts a left-handed spiral conformation. The C_α−C_α distances in the C^1−C^{15} and C^3−C^{11} disulfide bonds are 4.7 and 6.0 Å, respectively. The overall structure of this peptide is characteristic of the cystine-stabilized α-helical motif (CSH), which involves the C-X-C triplet of a β-strand bonded through two disulfide bridges to a C-X-X-X-C stretch of an α-helix (*12*) (Figure 3).

The C-terminus is stabilized by hydrogen bonds established between the carbonyl group of C^{15} and the amide proton of R^{-1}, and between the carbonyl group of V^{12} and the amide proton of H^{16}. The amino-terminal capping motif of the helix involves a hydrogen bond between the OD1 atom of D^8 and the amide proton of C^{11}.

Packing Analysis of a Dimeric Peptide. Of particular interest is the packing arrangement of the peptide molecules in the orthorhombic crystal form reported here, revealing a tight contact typically relevant to a dimeric molecule. The two peptides in the asymmetric unit are related by a

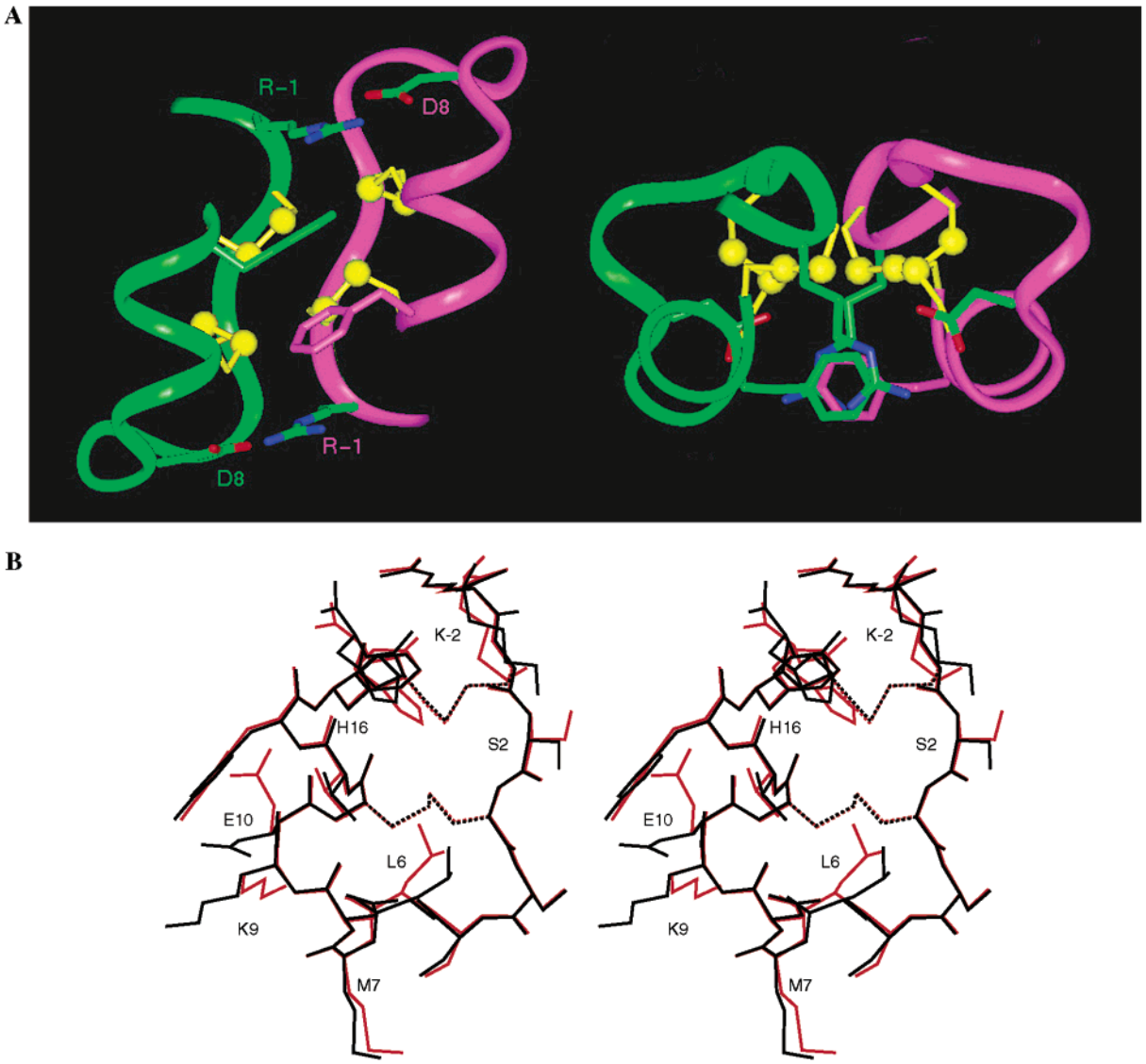

FIGURE 3: Schematic view of the KR-CSH-ET dimer and comparison of the structure of the two monomers. (A) Two views of the dimer that differ by a 90° rotation. At the left, the head-to-tail dimer forms a two-stranded antiparallel β-sheet involving residues C_1-C_3 of monomer A (green) and monomer B (purple). At the right, the groove between the monomers is filled by the disulfide bonds, the stacked F^{14} side chains located in the central part, and the two $R^{-1}-D^8$ intermolecular salt bridges located at each extremity. The dimer adopts a compact structure. The C^1-C^{15} and C^3-C^{11} disulfide bonds are colored yellow. (B) Stereoview of the superimposition of the two monomers. Monomers A and B are colored red and black, respectively. The minor alternate conformations of the S^2, S^5, M^7, and E^{10} side chains are not displayed. For clarity, only the side chains displaying a different orientation in the two monomers are labeled. The E^{10} side chain of the B monomer is involved in a salt bridge with the H^{16} side chain of the A monomer of the following asymmetric unit in the lattice. Disulfide bonds are represented with dotted lines.

noncrystallographic 2-fold axis ($\kappa = 179.8°$). The extensive contacts between the two molecules in the asymmetric unit involve the burying of large amounts of surface area (787 Å^2) at the interface between the monomers. This represents 27.7% of the total solvent accessible surface area of the dimer (2845 Å^2). All other intermolecular contacts between molecules do not involve such large contacts; buried contact areas are less than 240 Å^2/monomer, typical values for random packing interactions in crystals (*54*).

The interactions across the dimer interface are provided both by the formation of an antiparallel β-sheet between the β-strand of each monomer linked together by a standard pattern of four hydrogen bonds and by two salt bridges between R^{-1} and D^8 side chains (Figures 2B and 3). The homodimer is also stabilized by hydrophobic contacts between the side chains of C^1 and F^{14} of one monomer and C^{11} of the other monomer and also by the stacking of F^{14} rings (Figure 2A). In addition, four water molecules form hydrogen bonds with residues in both monomers, thus contributing to the hydrogen bonding network at the dimer interface. As indicated in Table 2, the two residues with the highest contribution to the buried interface area are R^{-1} and F^{14}.

The two monomers are well superimposed. A least-squares fit of the 18 C_α atoms of these two peptides gave an rmsd of 0.25 Å. Figures 3 and 4 show the resulting superposition of the two monomers. Only minor changes in the peptide backbone conformation of N- and C-terminal residues and the short loop segment (S^5-M^7) are observed. Both protomers exhibit different and extensive crystal packing environments that do not disturb the stable fold of the dimer. The comparison of the χ_1 angles reveals that a number of side chains switch between possible rotamers (S^2, S^5, M^7, K^9, and E^{10}). This results from different local packing interactions with symmetry-related molecules.

Table 2: Buried Area (square angstroms) of Selected Side Chains at the Interface of the KR-CSH-ET Dimer[a]

residue	monomer A	monomer B
K^{-2}	20	18
R^{-1}	98	91
C^{1}	36	39
S^{2}	39	38
S^{4}	51	49
D^{8}	35	38
E^{10}	18	21
C^{11}	29	29
F^{14}	65	65
C^{15}	5	3
total	396	391

[a] The calculation was carried out without the water molecules.

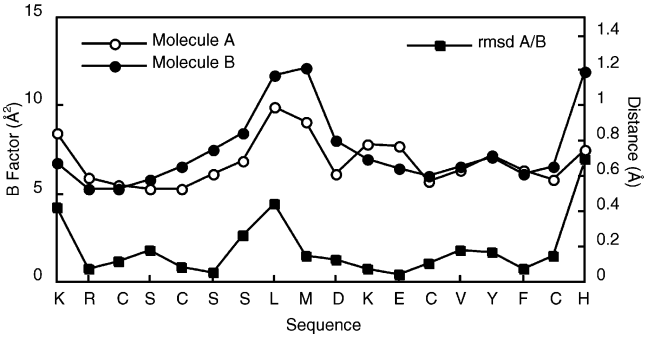

FIGURE 4: Average temperature factors (in square angstroms) for main chain atoms of the KR-CSH-ET monomers (○ for monomer A and ● for monomer B) as a function of residue number. Squares are for the distances (in angstroms) between corresponding C_α atoms after the superposition of chain B onto chain A.

Analysis of Temperature Factors. For each monomer, the mean temperature factors for the main chains atoms (6.8 and 7.6 Å^2) and side chain atoms (11.0 and 11.3 Å^2) are similar. As illustrated in Figure 4, they show a similar pattern of variation as a function of sequence, the higher *B* factors corresponding to the loop region (L^6 and M^7 residues) and to the C-terminal residue, H^{16} of the B monomer. The lower value measured for the H^{16} residue of the A monomer is consistent with its involvement in electrostatic interactions with the E^{10} side chain of a molecule belonging to another asymmetric unit. This $E^{10}-H^{16}$ intermolecular interaction explains the different orientation of the E^{10} side chain in the A and B monomers (Figure 3).

Anisotropic displacement parameters (ADPs) have been analyzed using PARVATI (*40*). The distribution of the anisotropy values for the 307 protein atoms shows a Gaussian shape with mean and σ values of 0.58 and 0.13, respectively. The mean anisotropy profile as a function of residue number is identical for the two molecules and relatively flat. The cysteine residues display low temperature factors and smaller mean anisotropies than the other residues.

Water Structure. Most of the resolved solvent molecules are in the first hydration shell and make hydrogen bonds with the dimer. Nearly half of the water molecules are found in pairs or networked with other waters (cutoff distance of 3.5 Å). There are five tightly bound water molecules found in monomers A and B with similar hydrogen bond connectivities. The three water molecules at the interface of the peptide dimer are involved in several hydrogen bonds, therefore contributing to the dimer stability. This is clearly the case for two of them, W^3 and $W^{3'}$, symmetrically located, which link together the R^{-1}(A) O, S^5(B) HN, and D^8(B) OD2 atoms and the R^{-1}(B) O, S^5(A) HN, and D^8(A) OD2 atoms, respectively (Table 3).

pH Dependency of the Dimerization. Sedimentation equilibrium experiments were carried out for both KR-ET-1 and KR-CSH-ET at three pH values (pH 1.4, 5.0, and 9.7) and over a concentration range of 0.1−4.0 mg/mL. The resulting apparent molecular masses of the peptides are reported in Table 4. These values clearly indicate that at pH 1.4 (where carboxyl groups are protonated) the two peptides are monomeric (theoretical averaged molecular masses of 2776.3 and 2134.5 Da for KR-ET-1 and KR-CSH-ET, respectively). In contrast, at pH 5.0 and 9.7 (where carboxyl groups are deprotonated), the apparent molecular masses of KR-ET-1 and KR-CSH-ET strongly suggest that the two peptides exist as dimers. Moreover, the apparent molecular masses remained unchanged in the concentration range of 0.1−4.0 mg/mL (Figure 5). This indicates, first, that the peptides do not aggregate at pH 1.4 and, second, that at pH 5.0 and 9.7, even at the highest concentrations, they do not form higher aggregates than the dimer, such as trimers or tetramers.

Dimers usually dissociate upon dilution. Interestingly, the KR-ET-1 and KR-CSH-ET dimers were still observed by ultracentifugation at concentrations as low as 0.1 mg/mL (0.050 mM). Likewise, NMR spectra recorded at a lower concentration (0.016 mM and pH 5.5) exhibited chemical

Table 3: Details of Interactions[a] between the Two Monomers in the KR-CSH-ET Dimer

monomer A	water molecule	monomer B	interactions	atoms involved	distance (Å)[b]
K^{-2}	–	S^4	H-bond	Omc (K^{-2})−OG (S^4)	2.66−2.76
R^{-1}	–	D^8	salt bridge	NE (R^{-1})−OD2 (D^8)	2.82−2.78
R^{-1}	–	D^8	salt bridge	NH2 (R^{-1})−OD1 (D^8)	2.87−2.89
R^{-1}	–	S^4	H-bond	Omc[c] (R^{-1})−Nmc (S^4)	2.92−2.97
R^{-1} (NH1)	w^1	E^{10} (OE1)	H-bond		
R^{-1} (NH2)	w^2	E^{10} (OE1)	H-bond		
R^{-1} (O)	w^3	D^8 (OD2)	H-bond		
S^2	–	S^2	H-bond	Omc (S^2)−Nmc (S^2)	2.92−2.89
S^4 (OG)	w^4	S^2 (OG)	H-bond		
C^{11}	–	C^1	hydrophobic	CB,SG (C^{11})−SG (C^1)	3.76−3.90
C^1	–	C^{15}	hydrophobic	SG (C^1)−SG (C^{15})	3.83−3.94
C^{11}	–	F^{14}	hydrophobic	CB,SG (C^{11})−CE2,CZ (F^{14})	4.09−4.13
F^{14}	–	F^{14}	hydrophobic	CE2−CD	3.70−3.70
				CZ−CG	4.18−4.28
				CE1−CD1	4.73−4.79

[a] Some interactions occur through a water molecule. [b] The distance range covers the distances measured in each monomer. [c] Omc and Nmc are for oxygen and nitrogen atoms of the main chain, respectively.

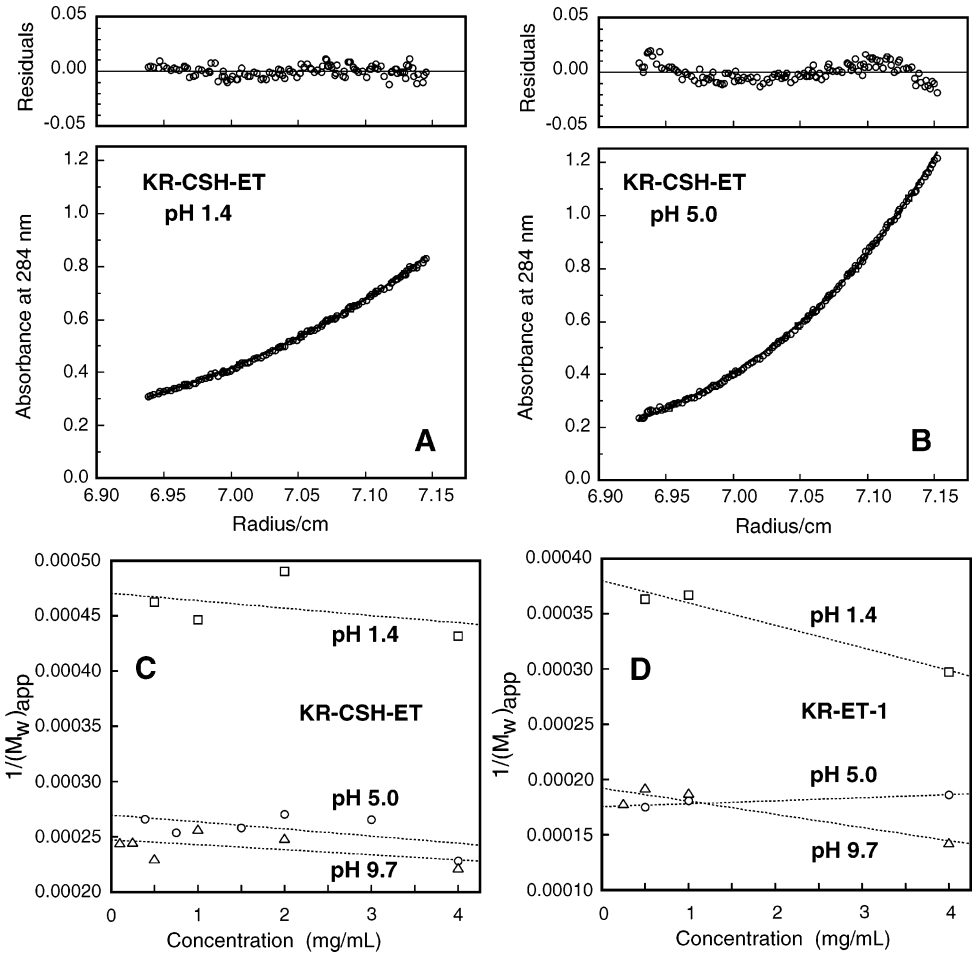

FIGURE 5: Apparent molecular mass measurements of KR-ET-1 and KR-CSH-ET by analytical ultracentrifugation experiments at different pH values and concentrations. Sedimentation equilibrium experiments were carried out for KR-CSH-ET (A) at pH 1.4 and (B) at pH 5.0 (1 mg/mL, 20 °C). (C) Graph showing the KR-CSH-ET apparent molecular mass [$(M_w)_{app}$] measured as a function of peptide concentration, in the range of 0.1−4.0 mg/mL, for three pH values. These data clearly show that the peptide exists as a dimer at pH 5.0 and 9.7 and as a monomer at pH 1.4. (D) A similar behavior was obtained with the KR-ET-1 peptide (see Table 4).

Table 4: Measurement by Ultracentrifugation of the KR-ET-1 and KR-CSH-ET Molecular Masses at Three pH Values and 20 °C

	KR-ET-1 ($\times 10^3$ Da)	KR-CSH-ET ($\times 10^3$ Da)
pH 1.4	2.63 ± 0.13	2.13 ± 0.1
pH 5.0	5.69 ± 0.28	3.71 ± 0.19
pH 9.7	5.19 ± 0.26	4.04 ± 0.2

shifts for aromatic protons typical of the dimer (see below), thus suggesting that even at very low concentrations the two peptides are still dimeric. This observation suggests that in the KR-ET-1 series the dimers display unusually high stabilities.

Stability of the R^{-1}−D^8 Salt Bridge in Molecular Dynamics Simulations. Since previous molecular dynamics simulations on monomeric KR-CSH-ET revealed a rather unstable intramolecular R^{-1}−D^8 salt bridge (*19*), we carried out similar simulations on dimeric KR-CSH-ET to check the stability of the intermolecular salt bridges. As previously done for the monomer, several simulations were performed using either the GB/SA implicit solvation scheme or explicit solvation and the particle-mesh Ewald summation method to evaluate long-range electrostatic interactions, using the dimeric X-ray structure reported here as the starting structure.

The deviation from the starting conformation remained well below 1.5 Å during the explicit solvent simulation, and the mean rmsd for all C_α atoms of the dimeric structure over the simulations was 0.99 Å with a standard deviation of 0.18 Å. This indicates that both the monomer and the dimer conformations were stable in the simulation. Similar results were obtained from the GB/SA simulations.

Distances between atoms of the R^{-1} and D^8 residues of the two monomers were used to monitor the intermolecular salt bridges along the simulations. As shown in Figure 6, these side chain interactions were conserved during the major part of the explicit solvent simulation. Interestingly, both salt bridges underwent significant conformational changes over the course of 1−2 ns, but the R^{-1}−D^8 interaction finally stabilized in a conformation very similar to the initial one. The temporary weakening of the salt bridges nevertheless allowed a 180° rotation of the D^8 χ_2 angle to occur in one salt bridge, thus interchanging the D^8 OD1 and OD2 atoms involved in the salt bridge.

Solution Structure of the Dimer. The X-ray structure was essential for reinterpreting NMR data and differentiating intermolecular and intramolecular NOEs in the dimer. Indeed, some side chains at the interface are involved in both intra- and intermolecular contacts, and without any knowledge of their relative arrangement, it would have been very difficult to correctly assign these NOEs. This is in particular the case for protons of the F^{14} ring. Indeed, due to the head-to-tail

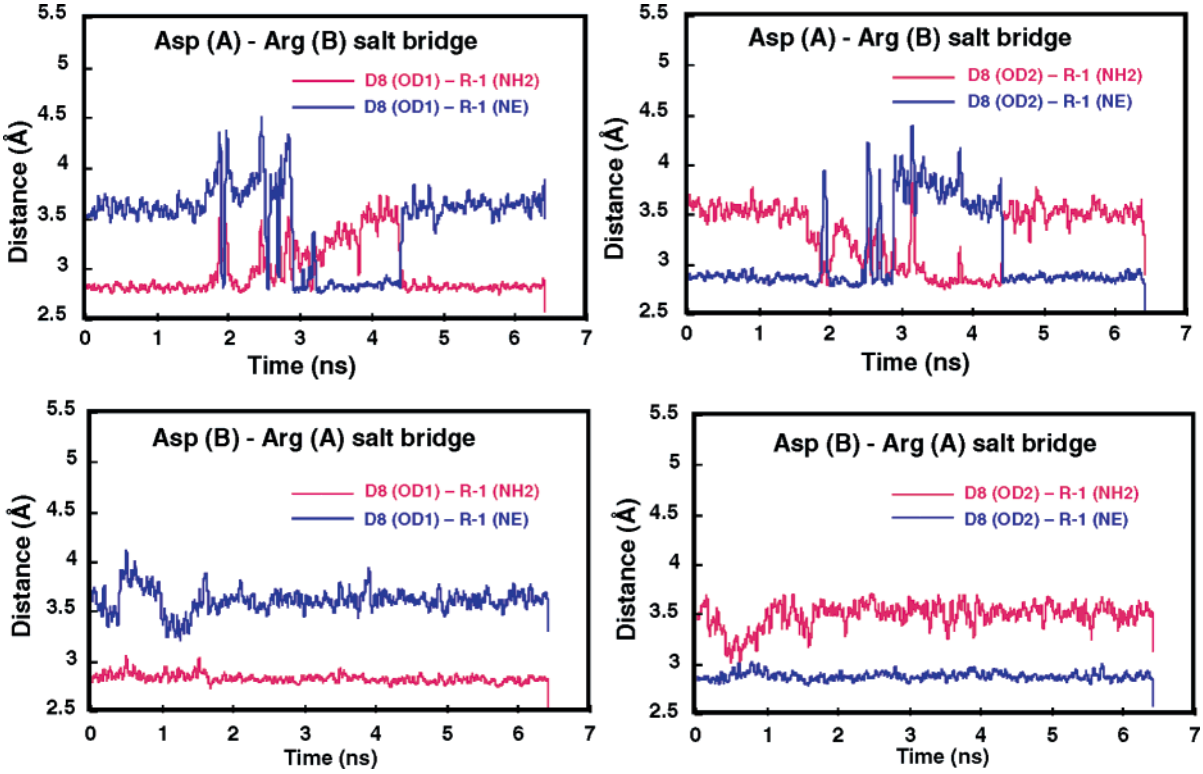

FIGURE 6: N−O distances measured for the $D^8(A)-R^{-1}(B)$ (top) and $D^8(B)-R^{-1}(A)$ (bottom) salt bridges of the crystal dimer all along the 6.5 ns molecular dynamics simulation using an explicit solvation. In the top graphs, notice the "slow" breakage and the "fast" reformation of the salt bridge without dissociation of the dimer. In the bottom graphs, the salt bridge is very stable all along the simulation. For the sake of clarity, distances were smoothed over a 15 ps window. Similar distance profiles were obtained with the GB/SA implicit solvation method (data not shown).

stacking of the F^{14} rings at the dimer interface, some protons of one monomer are simultaneously involved in intermolecular NOEs (for example, H4 and H3,5 protons with E^{10} and C^{11} side chain protons) and in intramolecular NOEs (H4 proton with R^{-1} Hδ protons). Similarly, in the interfacial β-sheet structure, the C^1 Hα proton is involved in both intermolecular (with C^3 Hα and S^4 HN protons) and intramolecular (with the S^2 HN proton) NOEs. Once intramolecular and intermolecular NOEs were identified (Figure 7), 484 NMR-derived constraints containing 38 intermolecular constraints were used to calculate a family of 10 conformers for the dimer using DYANA. The obtained structures were energy refined using AMBER (mean backbone rmsd of 0.57 ± 0.12 Å) and showed no violation larger than 0.2 Å. During the energy refinement calculation, the R^{-1} guanidine and carboxylate (D^8) groups reached a practically coplanar geometry very similar to that of the X-ray structure (Figure 8). The backbones of the solution and X-ray structures are very similar (mean backbone rmsd of 0.85 ± 0.08 Å). The higher mean rmsd value measured for the heavy atoms (1.65 ± 0.12 Å) is related to different orientations of K^{-2}, M^7, and Y^{13} side chains (Figure 8).

DISCUSSION

The structural studies of the KR-ET-1 and KR-SRTb peptides showed that the $R^{-1}-D^8$ salt bridge depends neither on the C-terminal sequence nor on the sequence of the S^4-M^7 loop. Such a C-terminal independency of the salt bridge was further confirmed by the study of the shortened KR-CSH-ET peptide (*19*). However, this salt bridge remained somewhat speculative since ^{1}H NMR experiments do not allow direct characterization of salt bridges. Therefore, the presence of the $R^{-1}-D^8$ salt bridge was inferred from

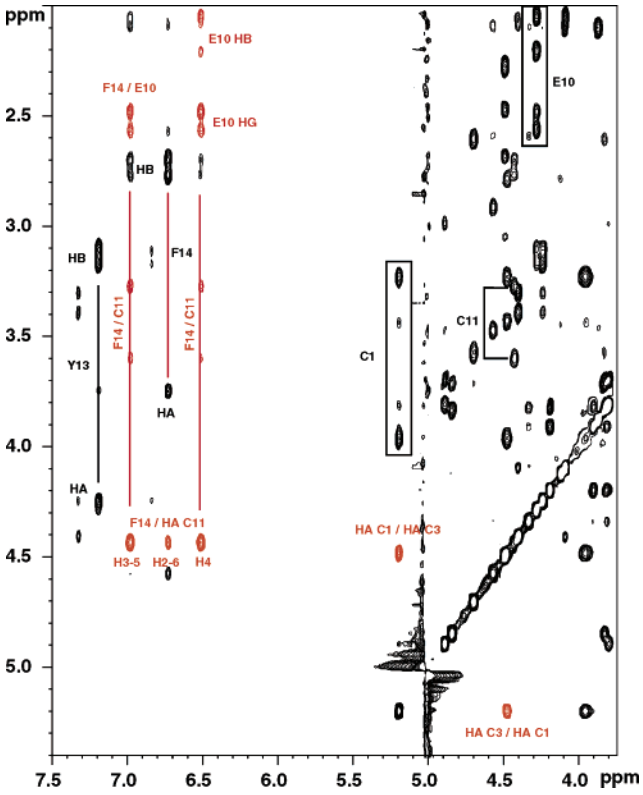

FIGURE 7: Selected part of the NOESY spectrum of KR-CSH-ET. The intermolecular NOE cross-peaks consistent with the crystallographic dimer are displayed and labeled in red (D_2O, 285 K, pH 3.9, 150 ms mixing time).

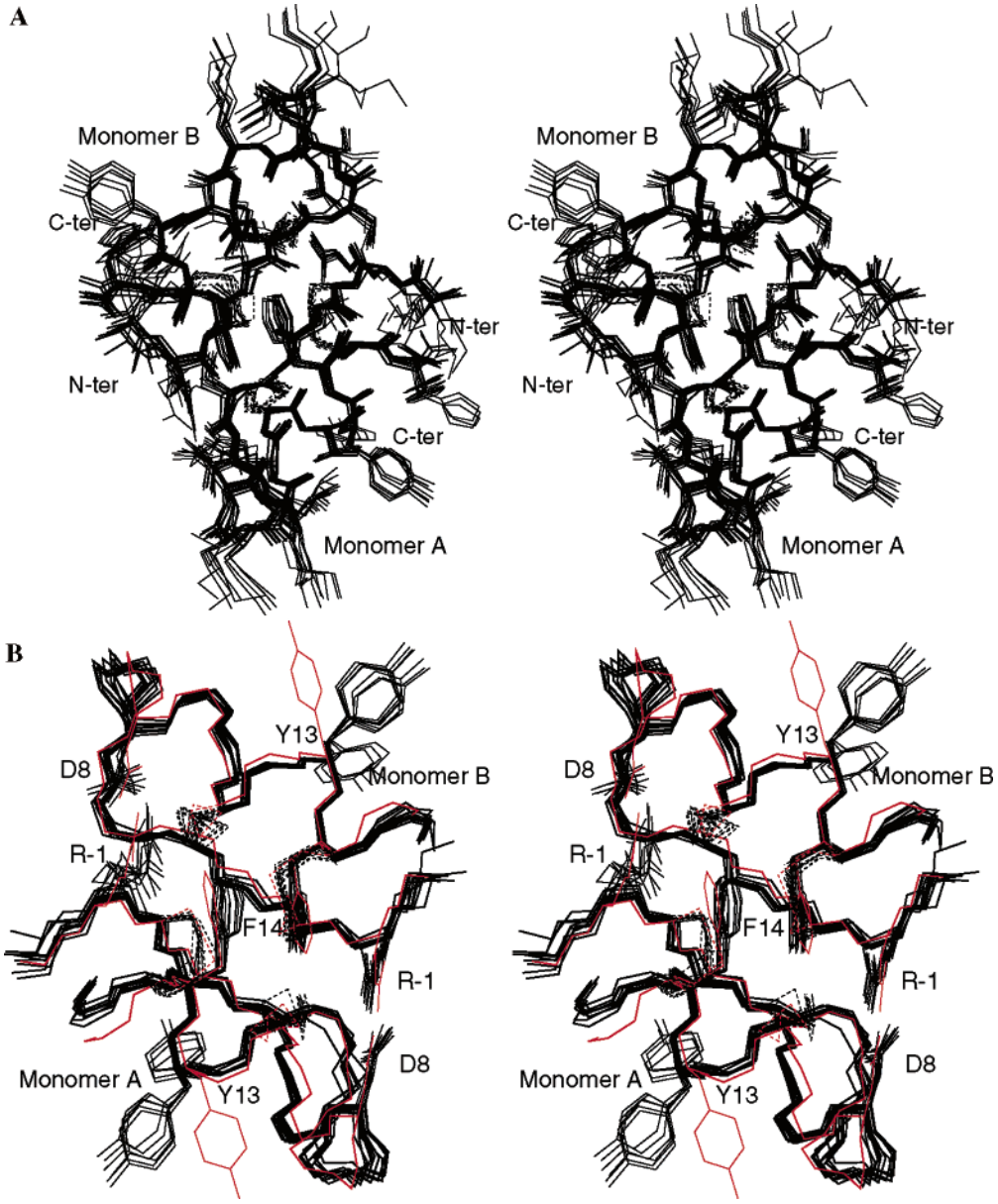

FIGURE 8: Comparison of the solution and crystal structures of the KR-CSH-ET dimer. (A) Stereoview of the 10 best energy-minimized conformers as determined from NMR-derived constraints (mean backbone rmsd of 0.57 ± 0.12 Å). (B) This stereoview turned by approximately 180° around the vertical axis shows the superimposition of the solution structures (black) with the crystal structure (red) (mean heavy atoms rmsd of 1.65 ± 0.12 Å). For clarity, only selected side chains (D^8, R^{-1}, Y^{13}, and F^{14}) are displayed. The disulfide bridges are displayed as dashed lines.

distance constraints in its vicinity and from the impact of point mutations. The study of the D^8N mutant of KR-ET-1 allowed us to unambiguously determine that electrostatic interactions occur between the R^{-1} and D^8 side chains. However, the stability of the proposed $R^{-1}-D^8$ salt bridge in KR-CSH-ET was questioned by molecular dynamics simulations (*19*). The apparent discrepancy between experimental data and simulations suggested either that the proposed structure was at least partly incorrect or that the force field did not appropriately estimate the stability of solvent-exposed salt bridges.

Therefore, to better characterize the $R^{-1}-D^8$ salt bridge, we started a crystallization project on the KR-CSH-ET peptide in the hope of determining its crystallographic structure, thus unambiguously ensuring the correct geometry of the $R^{-1}-D^8$ salt bridge. Medium-size peptides (8−25 residues) are known for their low propensity to crystallize. However, some of them, with or without disulfide bonds, were crystallized and their X-ray 3D structures determined (*55*, *56*). This is the case for ET-1 for which preliminary crystal data were reported in 1992 (*57*), and its X-ray structure was determined in 1994 at 2.18 Å resolution by using the molecular replacement technique (*10*). In this structure, the C-terminal tail is helical and thus significantly differs from those of all solution structures in which this part was found to be disordered.

Since ET-1, the parent peptide of KR-CSH-ET, was previously crystallized, the "more constrained" KR-CSH-ET peptide (two disulfide bonds and one salt bridge) was also expected to give crystals. Conditions of crystallization compatible with salt bridge formation (pH in the range of 4.6−5.6) were found, and diffraction-quality crystals were obtained. Because of the high resolution of the data, the structure was determined by the direct methods. Surprisingly,

in the crystal, KR-CSH-ET was found to be a highly symmetric dimer in which two $R^{-1}-D^{8}$ salt bridges do occur, but are intermolecular, in contrast to the previously inferred intramolecular salt bridge. For the two intermolecular salt bridges of the dimer [R^{-1}(A)$-D^{8}$(B) and R^{-1}(B)$-D^{8}$(A)], the R^{-1} and D^{8} side chains are almost perpendicular with quasi-coplanar carboxylate and guanidinium groups. The D^{8} OD2$-R^{-1}$ NE and D^{8} OD1$-R^{-1}$ NH2 distances lie in the range of 2.78−2.89 Å. Together, the quasi-coplanarity of the two charged groups along with the oxygen−nitrogen distances fully satisfies the geometrical requirements of a canonical salt bridge (*58*).

In agreement with our previous solution structures (*17*, *19*, *21*), the X-ray structure of KR-CSH-ET shows that the D^{8} side chain is involved in the N-capping of the helix (D^{8} OD1$-C^{11}$ N distance of 3.25−3.30 Å) and adopts a χ_1 value in the range of 174.3−178.3°. In contrast, the orientation of the R^{-1} side chains in the X-ray structure is clearly different from those previously reported. The main difference is for the χ_1 angle that is in the range of −172.3° to −172.5° in the X-ray structure, but +68° in the solution structure. As a result, the global fold of the A and B monomers and the orientation of the D^{8} side chain are very similar to those previously established for the solution structure, but the orientation of the R^{-1} side chain and the salt bridge itself strongly differ due to the incorrect intramolecular salt bridge in the solution structures.

It is striking that an incorrect intramolecular salt bridge could be easily introduced in the previously calculated solution structures without any severe constraints (*19*). It is likely that such a salt bridge was formed at the expense of some weak steric or internal strains in the peptide, thus explaining why it was rapidly broken in the simulations. Nevertheless, the intramolecular salt bridge was present in a large part of two of seven unrestrained GB/SA simulations, indicating that this salt bridge, although quite unstable, was not totally unrealistic (*19*). In contrast, the new simulations performed on the dimer were fully consistent with highly stable intermolecular salt bridges, since the salt bridges were maintained in all simulations. Therefore, our previous questioning about possible difficulties for the molecular mechanics force field in correctly accounting for the stability of solvent-exposed salt bridges now appears to be unfounded.

Structure of the Dimer Interface. The symmetric structure of the dimer interface mainly consists of a two-stranded β-sheet, two salt bridges, and a hydrophobic core. The intermolecular and symmetric β-sheet involving residues $R^{-1}-S^{4}$ of each monomer is stabilized by four hydrogen bonds [S^{4}(A) HN$-R^{-1}$(B) O, S^{2}(A) O$-S^{2}$(B) HN, S^{2}(A) HN$-S^{2}$(B) O, and R^{-1}(A) O$-S^{4}$(B) HN]. Two additional hydrogen bonds between the S^{4}(A) HG atom and the K^{-2}(B) O atom and between the S^{4}(B) HG atom and the K^{-2}(A) O atom also contribute to the stability of the β-sheet structure. Although to a lesser extent, the β-sheet is also indirectly stabilized by the R^{-1} HN$-C^{15}$ O intramolecular hydrogen bonds that contribute to the stabilization of the N- and C-terminal parts of each monomer.

The hydrophobic core mainly includes the four disulfide bonds, the head-to-tail stacked phenylalanine rings, and the hydrophobic part (β, γ, and δ atoms) of the arginine side chains (Figure 2). Moreover, the guanidinium group is almost coplanar with the phenylalanine ring at a distance compatible with cation$-\pi$ stabilizing interactions (3.5−4.5 Å) (*59*).

Overall, the dimer interface represents 27.7% (787 Å^2) of the total solvent accessible area of the dimer (2845 Å^2). Besides the β-sheet, it contains a network of stabilizing interactions successively including (from top to bottom in the left panel of Figure 3A) the first $R^{-1}-D^{8}$ salt bridge, the cation$-\pi$ interaction, the phenylalanine stacking in the middle, associated with hydrophobic contacts with and between disulfide bridges, and again the cation$-\pi$ interaction and the second salt bridge. The shape complementarity at the interface and the high density of stabilizing interactions are unique and provide this small peptide dimer with an unusually high stability.

The Dimer Is Stable in Solution. Since the crystal structure revealed a head-to-tail symmetric dimer stabilized by two intermolecular $R^{-1}-D^{8}$ salt bridges, we wondered whether such a dimer also exists in solution. To address this point, (i) ultracentrifugation experiments were carried out to measure the apparent molecular mass as a function of pH and (ii) NMR data were reinterpreted on the basis of the X-ray dimer structure.

Ultracentrifugation experiments unambiguously confirmed that KR-ET-1 and KR-CSH-ET have a dimeric quaternary structure in solution when carboxyl groups are deprotonated (pH 5.0 and 9.7), whereas monomers are observed when carboxyl groups are protonated (pH 1.4). On the basis of the hypothesis that the dimer in solution is similar to the dimer in the crystal, NMR data were reinterpreted. Few intermolecular NOEs consistent with the dimer were identified, and some of them are displayed in Figure 7. Both the C^{1} $H_\alpha-C^{3}$ H_α and the C^{1} $H_\alpha-S^{4}$ HN NOEs were systematically unsatisfied for the initial monomer, and were assumed to result from residual exchange between the major and minor conformers and thus were discarded in previous studies. Now, we see that these NOEs actually agree with the head-to-tail β-sheet of the dimer interface. All these protons belong to the two extremities of the symmetric and antiparallel β-sheet involving the $C^{1}-S^{4}$ segments of each monomer. Because of the symmetry, only these few interstrand NOEs (and their symmetrical counterparts) allow us to characterize the β-sheet interface. The NOEs involving S^{2} residues of the two monomers [S^{2}(A) $H_\alpha-S^{2}$(B) H_α (2.65 Å), S^{2}(A) $H_\alpha-S^{2}$(B) HN (3.2−3.5 Å), and S^{2}(A) HN$-S^{2}$(B) HN (2.75 Å)] should be observed, but due to S^{2} being in the middle of the β-sheet and the symmetry, the intermolecular and intramolecular NOEs could not be differentiated. Finally, the large values of the $^3J_{HN-H\alpha}$ coupling constants support the β-stranded structure for the $C^{1}-C^{3}$ fragment.

The NOEs involving protons of the F^{14} ring with both the C^{11} H_α and $H_{\beta\beta'}$ protons and those of the E^{10} side chain are in full agreement with the dimeric structure and correspond to intermolecular proximities. Indeed, in the dimer interface, the H4 and H3−5 protons of the F^{14} ring are close to both the C^{11} H_α proton and protons of the E^{10} side chain (Figure 7). Similarly, the intermolecular NOE between the R^{-1} HE atom and the C^{11} HB atom is also in full agreement with the crystallographic dimer. In the crystallographic monomers, all these distances are longer than 4.5 Å and thus are inconsistent with intramolecular NOEs. Notice that the small size of the molecule and the 2-fold symmetry of the dimer

explain why only few NOEs specific to the dimer are observed. In contrast, since they occur twice, these specific NOEs are rather intense.

In the dimer, the two helical structures spanning residues K^9-C^{15} are in contact via their disulfide bonds and their stacked F^{14} rings. Due to the very close chemical shifts for protons of each group, the cross-peaks corresponding to the expected intermolecular NOEs are too close to the diagonal to be identified and assigned. Although the amide proton of C^1 is not involved in the hydrogen bonds of the β-sheet, it was slowly exchanging. Examination of the X-ray and solution structures of the dimer revealed that this amide proton is buried and protected from the solvent by the backbone and the K^{-2} and R^{-1} side chains. The low solvent accessibility probably explains the slow exchange of this amide proton.

As a global result, both ultracentrifugation data as a function of pH and concentration and the NMR-derived structure allow us to conclude that a dimer similar to that determined by crystallography also exists in solution for pH values at which the carboxyl groups are deprotonated. Moreover, molecular dynamics simulations of the X-ray dimer clearly showed that although located at the surface, the two salt bridges are remarkably stable in solution. On the basis of the typical chemical shifts of aromatic signals, NMR data at a very low concentration (0.016 mM and pH 5.5) indirectly characterize the presence of the salt bridge, and consequently support the stability of the dimeric structure.

Small peptides scarcely form very stable dimers, or higher-order oligomers. Therefore, aggregation of poorly hydrophobic peptides has not been reported to date. Recently, a study dedicated to this phenomenon was carried out with the plant cyclotides kalata B1 and B2 (29 residues, three disulfide bonds) (*60*). Surprisingly, although the B1 and B2 sequences are very similar (82.8% identical), this study revealed that kalata B2 exists as an equilibrium mixture of the monomer, tetramer, and, possibly, higher-order oligomers, whereas kalata B1 is mainly monomeric. To explain such an oligomerization, the authors proposed the simultaneous involvement of hydrophobic interactions for one face and charge−charge interactions for the other face. It was hypothesized that intermolecular electrostatic interactions between the D^{25} and R^{24} side chains would occur twice at the interface in a way similar to what we demonstrate here for KR-CSH-ET.

Comparison of the KR-CSH-ET Crystal Structure with Related Structures. The global fold of the KR-CSH-ET crystal structure is similar to that previously established on the basis of NMR constraints (*19*). Nevertheless, the C_α superimposition of the X-ray A and B monomers onto a set of 40 solution structures resulted in a rather high average rmsd value (2.07 ± 0.14 Å). The largest contributions to this high value were from the N-terminal sequence and to a lesser extent from the C^{15} and H^{16} residues. In contrast, the C^3-F^{14} superimposition yielded a rmsd value of 0.58 ± 0.12 Å, indicating that for the major part of the sequence, the crystal structure reported here and previous solution structures are very similar, particularly in the S^4-M^7 loop region.

It is also interesting to compare the high-resolution structure of KR-CSH-ET with first the solution structure (PDB entry 1EDP) (*8*) and then with the crystal structure of the ET-1 parent peptide [PDB entry 1EDN (*10*)] (Figures 1 and 9).

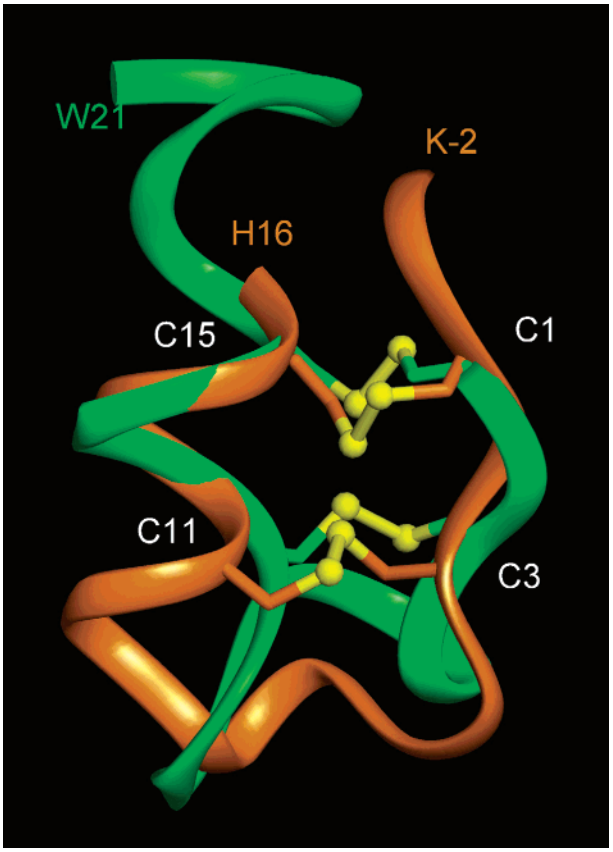

FIGURE 9: Comparison of the KR-CSH-ET (orange ribbon) and ET-1 [PDB entry 1EDN, (*10*) green ribbon] crystal structures. The backbone atoms of the C^1-C^3 and $C^{11}-C^{15}$ sequences were used for the superimposition (rmsd = 1.98 Å). The two structures mainly differ from the loop (residues 4−7), from the helix that is more regular for KR-CSH-ET, and from the disulfide bonds (see the text) displayed as balls and sticks.

The superimposition of residues 2−15 of the KR-CSH-ET crystal structure with those of the ET-1 solution structures (1EDP) revealed that the two backbones are similar (rmsd = 1.02 Å). In contrast, although disulfide bonds display a similar geometry, the high rmsd value measured for heavy atoms (3.58 Å) is indicative that several side chains are differently oriented in the two molecules.

KR-CSH-ET and ET-1 (PDB entry 1EDN) crystallized in two different space groups with comparable water content ($P2_12_12$ for KR-CSH-ET with 33% of the water and $P6_122$ for ET-1 with 36% of the water). The resolution for KR-CSH-ET is much better than that for ET-1 (1.13 Å compared to 2.18 Å). Although the two peptides share a helical structure (K^9-H^{16}), the helix of KR-CSH-ET is more regular than that of ET-1 (Figure 9). Despite a similar global fold, the superimposition of the backbone atoms of the C^1-C^{15} sequence yielded a rather high rmsd value of 2.55 Å (1.98 Å for the C^1-C^3 and $C^{11}-C^{15}$ superimposition). This high value indicates that although they display the same sequence, the global fold of these two peptides exhibits significant differences. This underlines the role of the additional constraints (salt bridges and crystal packing) in the alteration of the structure of this fold, although it is constrained by two disulfide bonds.

Significant differences between KR-CSH-ET and ET-1 crystal structures arise from the comparison of the disulfide bond geometries, those of KR-CSH-ET being much more canonical. For the A and B monomers, the χ_3 angles of the 1−15 disulfide bond are in the range of −94.5° to −98.2° with $C_\alpha-C_\alpha$ distances of 4.6−4.7 Å. These values have to be compared with a χ_3 angle of +143.8° and a distance of 6.16 Å for ET-1. Similarly, values for the χ_3 angle and the $C_\alpha-C_\alpha$ distance of the C^3-C^{11} disulfide (−103.5° to −101.7° and 6.0 Å, respectively) have to be compared to the values of −131.4° and 5.3 Å, respectively, measured for ET-1. Besides disulfide bonds, the superimposition of the two structures clearly revealed that the rotamer of Y^{13} is conserved ($\chi_1 = -60°$) while that of F^{14} is quite different (χ_1 equals 177° for KR-CSH-ET instead of −19° for ET-1) probably due to the dimerization.

Finally, the crystal packing environments of KR-CSH-ET and ET-1 are quite different; in the asymmetric unit of KR-CSH-ET, the dimer association is mediated by a two-stranded antiparallel β-sheet. In agreement with the statistical analysis of protein−protein interfaces by Jones and Thornton (*61*), this interface mainly involves hydrophobic residues, a single aromatic residue, several hydrogen bonds in a β-sheet structure, and a good shape complementarity.

In the case of ET-1, the asymmetric unit is a monomer and intermolecular contacts of two types were described (*10*). For the first one, the helices of the two neighboring molecules are nearly normal to each other and the buried surface area is ≈700 Å^2. For the second one, the helices run roughly parallel to each other in a "dimer-like" relationship with a buried surface area of ≈800 Å^2. Likewise for KR-CSH-ET, this latter dimer has a 2-fold symmetry axis with a comparable interface area (≈800 Å^2), but the interactions involved are quite different. Indeed, the W^{21} and Y^{13} side chains that contribute to this interface are absent and solvent-exposed in the KR-CSH-ET interface, respectively. Moreover, there is neither a salt bridge interaction nor main chain−main chain hydrogen bonds. The fact that intermolecular contacts are mainly hydrophobic is probably responsible for the high propensity of ET-1 to aggregate in water. To limit or avoid such an aggregation, various solvent mixtures were used for NMR structural studies. In contrast, for the KR-ET-1 and KR-CSH-ET peptides, besides the pH-mediated dimer described in this work, no aggregation was observed in aqueous solution.

Can the Salt-Bridged Dimer Favor the Formation of the Native Disulfide Bridges of KR-ET-1 and KR-CSH-ET? We have shown that the Lys-Arg dipeptide, which belongs to the ET-1 prosequence, significantly increased the yield of the native isomer. The oxidative folding reaction is carried out at pH 8.0−9.5, an experimental pH condition compatible with the formation of a stable dimer. It should be noted that the KR-ET-1 isomer with the non-native disulfide pattern did not experience significant alterations as a function of pH, such as the downfield shift of the HE proton of R^{-1}, suggesting that in this case the Arg side chain was not involved in a salt bridge (*21*).

Thus, the dimerization occurs for only the native disulfide isomer. It can be hypothesized that oxidative folding of KR-CSH-ET is thermodynamically controlled and that formation of the stable dimer drives the equilibrium to the native disulfide isomer. The $R^{-1}-D^8$ highly specific salt bridge is the main stabilizing element of the native dimer and could explain how the Lys-Arg dipeptide indirectly improves the yield in the native isomer. Moreover, the study of truncated KR-CSH-ET showed that the C-terminal part is not essential for salt bridge stability.

Biological Implications. As mentioned above, although the sequence of ET-1 is strictly conserved, its N-terminal extension by the Lys-Arg dipeptide of its prosequence yielded an analogue (KR-ET-1) whose vasoconstrictor activity is 540-fold less potent. One can also wonder if the dimerization could be responsible for such a vasoconstrictor potency decrease. For KR-ET-1, NMR data showed that the Lys-Arg dipeptide induced significant conformational alterations of the C-terminus which contains essential residues L^{17} and W^{21}, upon formation of the salt bridge and therefore of the dimer. Indeed, the γ-CH3 signal of I^{19} was particularly sensitive to the presence or absence of the salt bridge (*17*, *21*). However, the study of truncated KR-CSH-ET showed that the C-terminal part is not essential for salt bridge stability.

It is, nevertheless, possible that the full-length dimer (KR-ET-1) with a more constrained C-terminal tail could not be recognized by the receptor. Recognition of the dimer by the receptor may also be precluded either by steric hindrance or by burying residues important for receptor binding in the dimer interface. However, whether the dimer exists at a biological concentration, which is probably lower than that used for the physicochemical studies, or whether its dissociation constant has to be considered for receptor binding remains to be determined.

The KR-CSH-ET truncated peptide was more drastically modified since, in addition to the N-terminal extension, five C-terminal residues (including L^{17} and W^{21} residues which are essential for activity) were removed. Consequently, its vasoconstrictor activity, if any, is probably very low and was not measured. Therefore, the biological interest in the molecules discussed here is at the folding level and more precisely in the formation of the native disulfide bonds. Indeed, *in vitro*, the non-native ET-1 isomer, wich is inactive, is obtained in ≈25−30% yield. More generally, the pathway and factors that drive the folding of small disulfide-rich proteins to their bioactive three-dimensional arrangement are poorly understood and are the aim of many studies.

Interestingly, the prosequence fragment of human ET-1 spanning residues 20−52 contains 30% of the charged residues (five Glu's, four Arg's, and one Lys). Several prosequences with such a high content of charged residues have been proposed to play a significant role during the *in vivo* folding of several proteins, such as α-lytic protease, subtilisin, carboxypeptidase Y, and BPTI. This effect has sometimes been termed intramolecular chaperoning (*62*−*65*). Recently, Lauber et al. reported the structural study of the proguanylin and several mutants and showed that the N-terminal β-strand of the prosequence makes an essential contribution to the disulfide-coupled folding of the guanylin hormone (*66*).

Since the KR dipeptide at the N-terminus of the KR-CSH-ET peptide described here is present in the prosequence of the original ET-1 hormone, these upstream residues might play, *in vivo*, the role of an intramolecular chaperone.

CONCLUSION

Overall, this study underlines the interest in using several complementary techniques to address even apparently simple structural problems. In the folding context, the main point from our structural study is the experimental determination of electrostatic interactions, between a positively charged residue (Arg) belonging to the prosequence and a negatively charged residue (Asp) of ET-1, that are sufficiently strong to give rise to a very stable intermolecular salt bridge. Since disulfide bonds are formed in a thermodynamically controlled step, the stability provided by these two salt bridges to the native dimer would explain the improvement of the formation of this ET-1 isomer. From these results, it can be hypothesized that similar salt bridges between the prosequence and ET-1 might assist the formation of the native disulfide bonds during the *in vivo* folding before the successive cleavages that deliver the active hormone.

REFERENCES

1. Yanagisawa, M., Inoue, A., Ishikawa, T., Kasuya, Y., Kimura, S., Kumagaye, S., Nakajima, K., Watanabe, T. X., Sakakibara, S., Goto, K., and Masaki, T. (1988) Primary structure, synthesis, and biological activity of rat endothelin, an endothelium-derived vasoconstrictor peptide, *Proc. Natl. Acad. Sci. U.S.A. 85*, 6964−6967.
2. Yanagisawa, M., Kurihara, H., Kimura, S., Tomobe, Y., Kobayashi, M., Mitsui, Y., Yazaki, Y., Goto, K., and Masaki, T. (1988) A novel potent vasoconstrictor peptide produced by vascular endothelial cells, *Nature 332*, 411−415.
3. Itoh, Y., Yanagisawa, M., Ohkubo, S., Kimura, C., Kosaka, T., Inoue, A., Ishida, N., Mitsui, Y., Onda, H., Fujino, M., and Masaki, T. (1988) Cloning and sequence analysis of cDNA encoding the precursor of a human endothelium-derived vasoconstrictor peptide, endothelin: identity of human and porcine endothelin, *FEBS Lett. 231*, 440−444.
4. Kimura, S., Kasuya, Y., Sawamura, T., Shinimi, O., Sugita, Y., Yanagisawa, M., Goto, K., and Masaki, T. (1989) Conversion of big endothelin-1 to 21-residue endothelin-1 is essential for expression of full vasoconstrictor activity: structure−activity relationships of big endothelin-1, *J. Cardiovasc. Pharmacol. 13* (Suppl. 5), S5−S7, S18 (discussion).
5. Kumagaye, S., Kuroda, H., Nakajima, K., Watanabe, T. X., Kimura, T., Masaki, T., and Sakakibara, S. (1988) Synthesis and disulfide structure determination of porcine endothelin: an endothelium-derived vasoconstricting peptide, *Int. J. Pept. Protein Res. 32*, 519−526.
6. Aumelas, A., Chiche, L., Mahe, E., Le-Nguyen, D., Sizun, P., Berthault, P., and Perly, B. (1991) Determination of the structure of [Nle7]-endothelin by ^{1}H NMR, *Int. J. Pept. Protein Res. 37*, 315−324.
7. Tamaoki, H., Kobayashi, Y., Nishimura, S., Ohkubo, T., Kyogoku, Y., Nakajima, K., Kumagaye, S., Kimura, T., and Sakakibara, S. (1991) Solution conformation of endothelin determined by means of ^{1}H NMR spectroscopy and distance geometry calculations, *Protein Eng. 4*, 509−518.
8. Andersen, N. H., Chen, C. P., Marschner, T. M., Krystek, S. R., Jr., and Bassolino, D. A. (1992) Conformational isomerism of endothelin in acidic aqueous media: a quantitative NOESY analysis, *Biochemistry 31*, 1280−1295.
9. Hewage, C. M., Jiang, L., Parkinson, J. A., Ramage, R., and Sadler, I. H. (1997) Solution structure determination of endothelin-1 in methanol/water by NMR and molecular modelling methods, *J. Pept. Sci. 3*, 415−428.
10. Janes, R. W., Peapus, D. H., and Wallace, B. A. (1994) The crystal structure of human endothelin, *Nat. Struct. Biol. 1*, 311−319.
11. Kobayashi, Y., Takashima, H., Tamaoki, H., Kyogoku, Y., Lambert, P., Kuroda, H., Chino, N., Watanabe, T. X., Kimura, T., Sakakibara, S., and Moroder, L. (1991) The cystine-stabilized α-helix: a common structural motif of ion-channel blocking neurotoxic peptides, *Biopolymers 31*, 1213−1220.
12. Tamaoki, H., Miura, R., Kusunoki, M., Kyogoku, Y., Kobayashi, Y., and Moroder, L. (1998) Folding motifs induced and stabilized by distinct cystine frameworks, *Protein Eng. 11*, 649−659.
13. Tam, J. P., Liu, W., Zhang, J. W., Galantino, M., Bertolero, F., Cristiani, C., Vaghi, F., and de Castiglione, R. (1994) Alanine scan of endothelin: importance of aromatic residues, *Peptides 15*, 703−708.
14. Nakajima, K., Kubo, S., Kumagaye, S., Nishio, H., Tsunemi, M., Inui, T., Kuroda, H., Chino, N., Watanabe, T. X., Kimura, T., and Sakakibara, S. (1989) Structure−activity relationship of endothelin: importance of charged groups, *Biochem. Biophys. Res. Commun. 163*, 424−429.
15. Kubo, S., Chino, N., Nakajima, K., Aumelas, A., Chiche, L., Segawa, S., Tamaoki, H., Kobayashi, Y., Kimura, T., and Sakakibara, S. (1997) Improvement in the oxidative folding of endothelin-1 by a Lys-Arg extension at the amino terminus: Implication of a salt bridge between Arg-1 and Asp8, *Lett. Pept. Sci. 4*, 185−192.
16. Nakajima, K., Kumagaye, S., Nishio, H., Kuroda, H., Watanabe, T. X., Kobayashi, Y., Tamaoki, H., Kimura, T., and Sakakibara, S. (1989) Synthesis of endothelin-1 analogues, endothelin-3, and sarafotoxin S6b: structure−activity relationships, *J. Cardiovasc. Pharmacol. 13*, S8−S12.
17. Aumelas, A., Chiche, L., Kubo, S., Chino, N., Tamaoki, H., and Kobayashi, Y. (1995) [Lys(−2)-Arg(−1)]endothelin-1 solution structure by two-dimensional ^{1}H NMR: possible involvement of electrostatic interactions in native disulfide bridge formation and in biological activity decrease, *Biochemistry 34*, 4546−4561.
18. Aumelas, A., Chiche, L., Kubo, S., Chino, N., Watanabe, T. X., and Kobayashi, Y. (1999) The chimeric peptide [Lys(−2)-Arg(−1)]-sarafotoxin-S6b, composed of the endothelin pro-sequence and sarafotoxin, retains the salt-bridge staple between Arg(−1) and Asp8 previously observed in [Lys(−2)-Arg(−1)]-endothelin. Implications of this salt-bridge in the contractile activity and the oxidative folding reaction, *Eur. J. Biochem. 266*, 977−985.
19. Kaas, Q., Aumelas, A., Kubo, S., Chino, N., Kobayashi, Y., and Chiche, L. (2002) The [Lys(−2)-Arg(−1)-des(17−21)]-endothelin-1 peptide retains the specific Arg(−1)-Asp8 salt bridge but reveals discrepancies between NMR data and molecular dynamics simulations, *Biochemistry 41*, 11099−11108.
20. Liu, A., Hu, W., Majumdar, A., Rosen, M. K., and Patel, D. J. (2000) NMR detection of side-chain-side-chain hydrogen bonding interactions in ^{13}C/^{15}N-labeled proteins, *J. Biomol. NMR 17*, 305−310.
21. Aumelas, A., Kubo, S., Chino, N., Chiche, L., Forest, E., Roumestand, C., and Kobayashi, Y. (1998) Formation of native disulfide bonds in endothelin-1. Structural evidence for the involvement of a highly specific salt bridge between the prosequence and the endothelin-1 sequence, *Biochemistry 37*, 5220−5230.
22. Plateau, P., and Guéron, M. (1982) Exchangeable proton NMR without base-line distortion, using new strong-pulse sequences, *J. Am. Chem. Soc. 104*, 7310−7311.
23. Piotto, M., Saudek, V., and Sklenar, V. (1992) Gradient-tailored excitation for single-quantum NMR spectroscopy of aqueous solutions, *J. Biomol. NMR 2*, 661−665.
24. Otwinowski, Z. (1993) *Data Collection and Processing*, Science and Engineering Research Council, Daresbury Laboratory, Warrington, U.K.
25. Collaborative Computational Project, Number 4 (1994) The CCP4 suite: programs for protein crystallography, *Acta Crystallogr. D50*, 760−763.
26. Navaza, J. (1994) AMoRe: an automated package for molecular replacement, *Acta Crystollog. A50*, 157−163.
27. Vagin, A., and Teplyakov, A. (1997) MOLREP: An Automated Program for Molecular Replacement, *J. Appl. Crystallogr. 30*, 1022−1025.
28. Kissinger, C. R., Gehlhaar, D. K., and Fogel, D. B. (1999) Rapid automated molecular replacement by evolutionary search, *Acta Crystallogr. D55*, 484−491.
29. Weeks, C. M., DeTitta, G. T., Miller, R., and Hauptman, H. A. (1993) Application of the minimal principle to peptide structures, *Acta Crystallogr. D49*, 179−181.
30. Miller, R., DeTitta, G. T., Jones, R., Langs, D. A., Weeks, C. M., and Hauptman, H. A. (1993) On the application of the minimal principle to solve unknown structures, *Science 259*, 1430−1433.

31. Weeks, C. M., and Miller, R. (1999) Optimizing Shake-and-Bake for proteins, *Acta Crystallogr. D55*, 492−500.
32. Blessing, R. H., and Smith, G. D. (1999) Difference structure-factor normalization for heavy-atom or anomalous-scattering substructure determinations, *J. Appl. Crystallogr. 32*, 664−670.
33. Perrakis, A., Morris, R., and Lamzin, V. S. (1999) Automated protein model building combined with iterative structure refinement, *Nat. Struct. Biol. 6*, 458−463.
34. Murshudov, G. N., Vagin, A. A., and Dodson, E. J. (1997) Refinement of macromolecular structures by the maximum-likelihood method, *Acta Crystallogr. D53*, 240−255.
35. Brunger, A. T. (1992) Free *R* value: a novel statistical quantity for assessing the accuracy of crystal structures, *Nature 355*, 472−474.
36. Jones, T. A., and Kjeldgaard, M. (1997) Electron-density map interpretation, *Methods Enzymol. 277*, 173−208.
37. Read, R. J. (1997) Model phase: probabilities and bias, *Methods Enzymol. 277*, 110−128.
38. Laskowski, R. A., Rullmannn, J. A., MacArthur, M. W., Kaptein, R., and Thornton, J. M. (1996) AQUA and PROCHECK-NMR: programs for checking the quality of protein structures solved by NMR, *J. Biomol. NMR 8*, 477−486.
39. Vaguine, A. A., Richelle, J., and Wodak, S. J. (1999) SFCHECK: a unified set of procedures for evaluating the quality of macromolecular structure-factor data and their agreement with the atomic model, *Acta Crystallogr. 55*, 191−205.
40. Merritt, E. A. (1999) Expanding the model: anisotropic displacement parameters in protein structure refinement, *Acta Crystallogr. D55*, 1109−1117.
41. Cohn, E. J., and Edsall, J. T. (1943) *Proteins, Amino Acids and Peptides as Ions and Dipolar Ions*, Reinhold, New York.
42. Schachman, H. K. (1959) *Ultracentrifugation in Biochemistry*, Academic Press, New York.
43. McRorie, D. K., and Voelker, P. J. (1993) *Self-Associating Systems in the Analytical Ultracentrifuge*, Beckman Instruments, Inc., Palo Alto, CA.
44. Laue, T. M. (1995) *Methods in Enzymology*, Vol. 259, pp 427−452, Academic Press, New York.
45. Guntert, P., Mumenthaler, C., and Wuthrich, K. (1997) Torsion angle dynamics for NMR structure calculation with the new program DYANA, *J. Mol. Biol. 273*, 283−298.
46. Frishman, D., and Argos, P. (1995) Knowledge-based protein secondary structure assignment, *Proteins 23*, 566−579.
47. Case, D. A., Pearlman, D. A., Caldwell, J. W., Cheatham, T. E., Wang, J., Ross, W. S., Simmerling, C. L., Darden, T. A., Merz, K. M., Stanton, R. V., Cheng, A. L., Vincent, J. J., Crowley, M., Tsui, V., Gohlke, H. V., Radmer, R. J., Duan, Y., Pitera, J., Massova, I., Seibel, G. L., Singh, U. C., Weiner, P. K., and Kollman, P. A. (2002) *AMBER 7*, University of California, San Francisco.
48. Cornell, W. D., Cieplak, P., Bayly, C. I., Gould, I. R., Merz, K. M., Jr., Ferguson, D. M., Spellmeyer, D. C., Fox, T., Caldwell, J. W., and Kollman, P. A. (1995) A Second Generation Force Field for the Simulation of Proteins, Nucleic Acids, and Organic Molecules, *J. Am. Chem. Soc. 117*, 5179−5197.
49. Tsui, V., and Case, D. A. (2000) Molecular Dynamics Simulations of Nucleic Acids with a Generalized Born Solvation Model, *J. Am. Chem. Soc. 122*, 2489−2498.
50. Jorgensen, W. L., Chandreskhar, J., Madura, J. D., Imprey, R. W., and Klein, M. L. (1983) Comparison of simple potential functions for simulating liquid water, *J. Chem. Phys. 79*, 926−935.
51. Berendsen, H. J. C., Postma, J. P. M., van Gunsteren, W. F., DiNola, A., and Haak, J. R. (1984) Molecular dynamics with coupling to an external bath, *J. Chem. Phys. 81*, 3684−3690.
52. Darden, T. A., York, D., and Pedersen, L. (1993) Particle mesh Ewald: An N·log(N) method for Ewald sums in large systems, *J. Chem. Phys. 98*, 10089−10092.
53. van Gunsteren, W. F., and Berendsen, H. J. C. (1977) Algorithms for macromolecular dynamics and constraints dynamics, *Mol. Phys. 34*, 1311−1327.
54. Janin, J., and Rodier, F. (1995) Protein−protein interaction at crystal contacts, *Proteins 23*, 580−587.
55. Bunkoczi, G., Schiell, M., Vertesy, L., and Sheldrick, G. M. (2003) Crystal structures of cephaibols, *J. Pept. Sci. 9*, 745−752.
56. Chugh, J. K., Bruckner, H., and Wallace, B. A. (2002) Model for a helical bundle channel based on the high-resolution crystal structure of trichotoxin_A50E, *Biochemistry 41*, 12934−12941.
57. Wolff, M., Day, J., Greenwood, A., Larson, S., and McPherson, A. (1992) Crystallization and preliminary X-ray analysis of human endothelin, *Acta Crystallogr. B48*, 239−240.
58. Creighton, T. E. (1993) *Proteins, Structures and Molecular Properties*, 2nd ed., W. H. Freeman, New York.
59. Ma, J. C., and Dougherty, D. A. (1997) The cation-p interaction, *Chem. Rev. 97*, 1303−1324.
60. Nourse, A., Trabi, M., Daly, N. L., and Craik, D. J. (2004) A comparison of the self-association behavior of the plant cyclotides kalata B1 and kalata B2 via analytical ultracentrifugation, *J. Biol. Chem. 279*, 562−570.
61. Jones, S., and Thornton, J. M. (1995) Protein−protein interactions: a review of protein dimer structures, *Prog. Biophys. Mol. Biol. 63*, 31−65.
62. Winther, J. R., and Sorensen, P. (1991) Propeptide of carboxypeptidase Y provides a chaperone-like function as well as inhibition of the enzymatic activity, *Proc. Natl. Acad. Sci. U.S.A. 88*, 9330−9334.
63. Shinde, U., and Inouye, M. (1993) Intramolecular chaperones and protein folding, *Trends Biochem. Sci. 18*, 442−446.
64. Price-Carter, M., Gray, W. R., and Goldenberg, D. P. (1996) Folding of ω-conotoxins. 1. Efficient disulfide-coupled folding of mature sequences in vitro, *Biochemistry 35*, 15537−15546.
65. Price-Carter, M., Gray, W. R., and Goldenberg, D. P. (1996) Folding of ω-conotoxins. 2. Influence of precursor sequences and protein disulfide isomerase, *Biochemistry 35*, 15547−15557.
66. Lauber, T., Schulz, A., Rosch, P., and Marx, U. C. (2004) Role of disulfide bonds for the structure and folding of proguanylin, *Biochemistry 43*, 10050−1057.

BI049098A